KeAi

CHINESE ROOTS
GLOBAL IMPACT

Contents lists available at ScienceDirect

Petroleum Science

journal homepage: www.keaipublishing.com/en/journals/petroleum-science



Original Paper

Analysis of seismic dispersion and attenuation for gas-hydrate formations in the South China Sea



Zuo-Xiu He ^a, Feng Zhang ^{a,*}, Pin-Bo Ding ^a, Xiang-Yang Li ^{a,b}, Hai-Feng Chen ^b

- ^a State Key Laboratory of Petroleum Resource and Engineering, China University of Petroleum (Beijing), Beijing, 102249, China
- ^b BGP Inc., China National Petroleum Corporation, Zhuozhou, 072750, Hebei, China

ARTICLE INFO

Article history: Received 13 November 2024 Received in revised form 3 February 2025 Accepted 13 May 2025 Available online 15 May 2025

Edited by Meng-Jiao Zhou

Keywords:
Gas hydrate-bearing formation
Rock physics model
Seismic velocity dispersion
Attenuation
Occurrence state
Seismic forward modeling

ABSTRACT

Existing studies indicate that gas hydrate-bearing formations exhibit notable seismic velocity dispersion and attenuation. The Shenhu area of the South China Sea hold significant gas hydrate resource potential; however, the relationship between seismic velocity dispersion, attenuation properties, and gas-hydrate saturation remains insufficiently understood. Furthermore, a significant mismatch exists between the real seismic angle gather near a well and the synthetic angle gather generated using the convolution method, and this discrepancy may arise from the seismic velocity dispersion and attenuation characteristics of the gas hydrate-bearing formations. In this paper, we develop a rock physics model that integrates White's and Dvorkin's models, accounting for varied types of gas-hydrate occurrence states, specifically tailored to the gas hydrate-bearing formations in the Shenhu area. This model is calibrated with well log data and employed to investigate how gas-hydrate saturation influences seismic velocity dispersion and attenuation. Numerical analysis reveals the coexistence of two types of gas-hydrate occurrence states in the region: high gas-hydrate saturation formations are dominated by loadbearing-type gas hydrate, and formations containing both gas hydrate and free gas may exhibit either load-bearing or pore-filling types. The seismic velocity dispersion and attenuation properties vary significantly depending on the gas-hydrate occurrence state. We further apply the proposed model to generate seismic velocity and attenuation logs at various frequencies. These logs are used in seismic forward modeling employing both the convolution method and the propagator matrix method. Well tie analysis indicates that the synthetic angle gather incorporating attenuation via the propagator matrix method aligns more closely with the real seismic angle gather than the convolution method. This study provides valuable insights into frequency-dependent amplitude versus offset (AVO) analysis and the seismic interpretation of gas hydrate-bearing formations in the South China Sea.

© 2025 The Authors. Publishing services by Elsevier B.V. on behalf of KeAi Communications Co. Ltd. This is an open access article under the CC BY-NC-ND license (http://creativecommons.org/licenses/by-nc-nd/4.0/).

1. Introduction

Natural gas hydrate is a crystalline substance resembling ice, composed of hydrocarbon gas molecules encased within water molecules (Bai et al., 2022; Merey and Chen, 2022; Su et al., 2022). It forms under conditions of high pressure and low temperature (Tian et al., 2021; Farhadian et al., 2023; Gu et al., 2024). Often referred to as "combustible ice", gas hydrate is a clean energy source with substantial reserves, holding potential as a significant energy resource in the future (Ye et al., 2020; Wei et al., 2021;

* Corresponding author. E-mail address: zhangfeng@cup.edu.cn (F. Zhang). Wang et al., 2023). Prospecting explorations indicate that significant amounts of gas hydrate are present in the South China Sea (Ning et al., 2020; He et al., 2022; Jin et al., 2023).

Research has demonstrated that gas hydrate-bearing formations exhibit seismic velocity dispersion and attenuation, with variations observed across different regions (Guerin and Goldberg, 2002; Sain and Singh, 2011; Wang and Wu, 2016; Ji et al., 2021; Wu et al., 2022; Santos et al., 2023; Liu et al., 2024b). Zhan et al. (2022) reported significant seismic velocity dispersion in gas hydrate-bearing and free gas-bearing formations in the Shenhu area. However, contradictory findings have emerged from other studies: Li et al. (2013) and Li and Liu (2017) suggested that gas hydrate decreases attenuation in the Shenhu area, while Zhang et al. (2016) reported an increase. Therefore, the relationship between seismic velocity

dispersion, attenuation, and gas-hydrate saturation in the Shenhu area remains ambiguous and warrants further investigation.

Rock physics models play a crucial role in exploring the relationship between seismic velocity dispersion, attenuation, and gas-hydrate saturation. Zhan et al. (2022) utilized the Hydrate-Bearing Effective Sediment (HBES) model to simulate formations with mixed gas-hydrate occurrence states in the Shenhu area, with the simulated curves aligning closely with well logs. Other rock physics models, despite lacking real data, have been employed to analyze the seismic properties of gas hydrate-bearing formations in the South China Sea. For instance, Li et al. (2013), Li (2015), and Li and Liu (2017) applied the Biot-Squirt (BISQ) model and White's model, while Zhang et al. (2016) combined effective medium theory with the BISQ model, resulting in differing outcomes. Dai et al. (2018) employed White's model and a double-porosity model to simulate various gas-hydrate occurrence states in the Dongsha area, revealing that attenuation initially increased and then decreased with the increase of gas-hydrate saturation at 30 Hz, with fracture-filling-type gas hydrate-bearing formations exhibiting higher attenuation. Wang (2022) combined the Krief model and the BISQ model for simulations in the Shenhu area, indicating that P-wave velocity and attenuation are sensitive to gas-hydrate saturation. In summary, gas-hydrate occurrence state significantly influences the relationship between seismic velocity dispersion, attenuation, and gas-hydrate saturation.

Seismic forward modeling and well tie analyses have been conducted for gas hydrate-bearing formations in the South China Sea (Wang et al., 2013; Zhou et al., 2022; Liu et al., 2024a). Some studies have designed models to simulate bottom simulating reflectors (BSR) and compared the simulated AVO curves with real data (Niu et al., 2006; Ruan et al., 2006; Xu et al., 2014; Liang et al., 2020; Zhang et al., 2021, 2024). Li (2021) employed reflectivity methods to generate synthetic gathers for gas-hydrate thin interbedded models, considering the impact of gas-hydrate saturation

but excluding seismic velocity dispersion and attenuation. Although seismic forward modeling using the propagator matrix method has incorporated these properties (Guo et al., 2016; Pang et al., 2018), few studies have applied this approach to gas hydrate-bearing formations.

In this paper, we conduct rock physics modeling and propagator matrix method based seismic forward modeling, taking into account the seismic velocity dispersion and attenuation properties of gas hydrate-bearing formations in the Shenhu area of the South China Sea. We first develop a rock physics model that integrates White's and Dvorkin's models to account for varied types of gashydrate occurrence states. This model is calibrated with well log data and employed to investigate how gas-hydrate saturation influences seismic velocity dispersion and attenuation. Subsequently, we perform seismic forward modeling based on the propagator matrix method to generate synthetic angle gathers incorporating attenuation. We then compare these gathers with the real seismic angle gather near a well and the synthetic angle gather generated using the convolution method. The aim of this study is to facilitate frequency-dependent AVO analysis and the seismic interpretation of gas hydrate-bearing formations in the South China Sea.

2. Analysis of well logs and seismic data

This study focuses on the Shenhu area of the Pearl River Mouth Basin in the South China Sea. The target gas-hydrate reservoir is categorized into three types (Fig. 1(a)): (1) the gas hydrate-bearing formation, which contains both water and gas hydrate; (2) the mixed formation, which contains water, gas hydrate, and free gas; (3) the free gas-bearing formation, which contains water and free gas (Li et al., 2018; Wang et al., 2021b, 2025; Zhou et al., 2022).

Fig. 1 presents the logs of well W17 in the Shenhu area, and the P- and S-wave velocities logs, as well as density log, are shown in

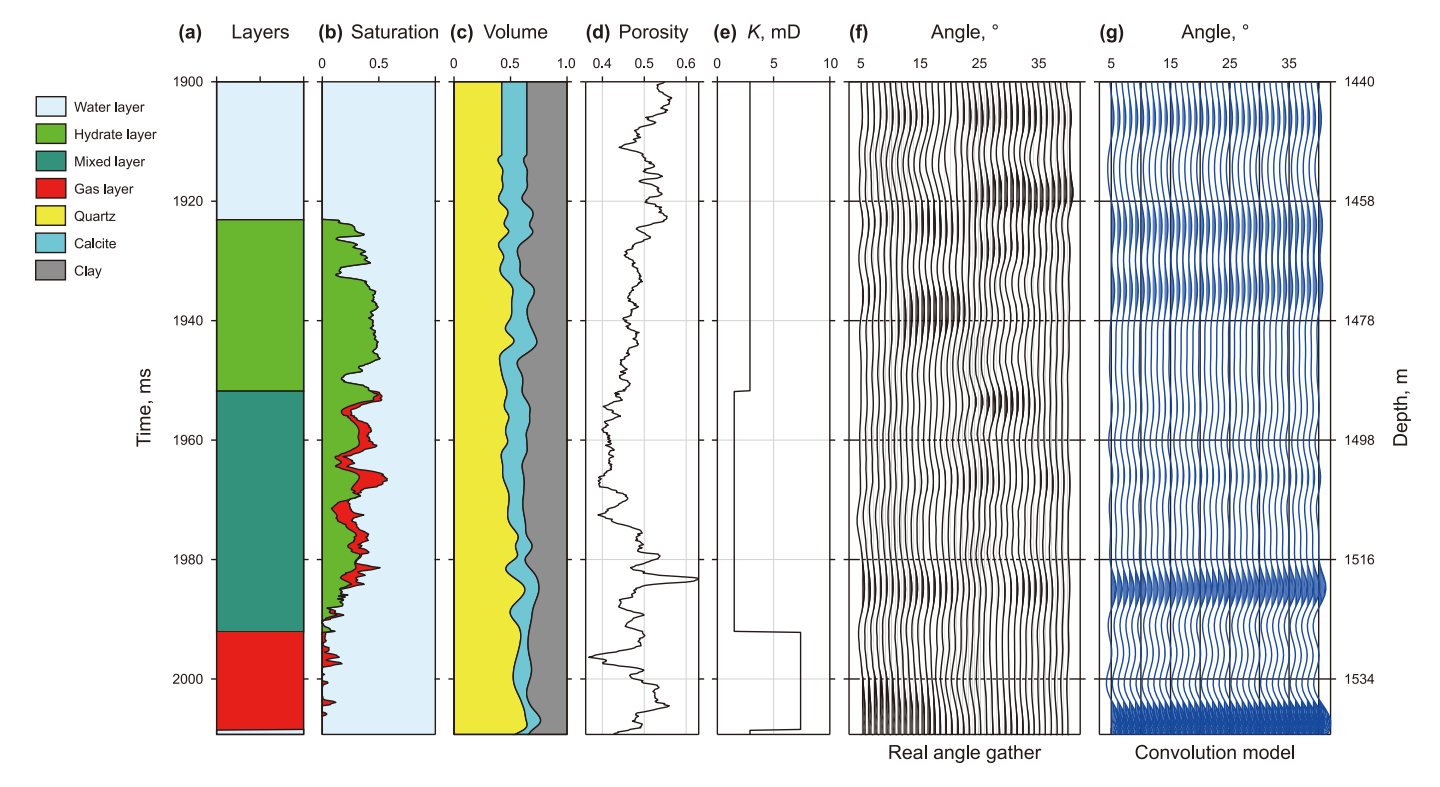


Fig. 1. (a) Geological interpretation of well W17, and logs of well W17: (b) saturation, (c) volume percentage of minerals from Yang et al. (2017), (d) porosity, (e) permeability from Li et al. (2018) and Chen et al. (2020). (f) Real seismic angle gather near a well and (g) synthetic angle gather generated using the convolution method.

Fig. 9. It should be noted that saturation is estimated based on the saturation logs from Xie et al. (2022). The volume percentage of minerals below 1450 m is derived from Yang et al. (2017), while the values above 1450 m are empirical estimates. Porosity is calculated from density, and permeability is derived from Li et al. (2018) and Chen et al. (2020).

We perform a well tie by comparing the real seismic angle gather near a well (Fig. 1(f)) with the synthetic angle gather generated using the convolution method (Fig. 1(g)). The comparison reveals that the locations of events in both angle gathers are generally consistent. However, a significant mismatch exists between the two, possibly due to abnormal amplitude variations in the real seismic angle gather or the absence of clear AVO characteristics in the synthetic angle gather. Additionally, this discrepancy may also result from the effects of velocity dispersion and attenuation in the gas hydrate-bearing formations.

3. Rock physics modeling for gas hydrate-bearing formations

3.1. Gas-hydrate occurrence states of gas hydrate-bearing formations

In the Shenhu area, gas hydrate coexists with free gas, as illustrated by the core sample presented by Liu et al. (2017) (Fig. 2). Given this coexistence, rock physics investigations typically identify four types of gas-hydrate occurrence states: (1) pore-filling type (Fig. 3(a)), (2) load-bearing type (Fig. 3(b)), (3) contact-cementing type (Fig. 3(c)), and (4) envelope-cementing type (Fig. 3(d)) (Wang et al., 2021a). These occurrence states will be taken into account in the subsequent rock physics modeling.

3.2. Rock physics modeling method for gas hydrate-bearing formations

In this section, we present several rock physics models that combine White's model with Dvorkin's effective medium model and cementation model, respectively, to analyze formations containing gas hydrate at different occurrence states in the Shenhu area. Fig. 4 illustrates the workflow of the rock physics modeling for pore-filling-type, load-bearing-type and cementing-type gas hydrate-bearing formations, respectively. Specifically, the texts on a white background represent common components of rock physics modeling, while the texts on a grey background at the top,

middle and bottom pertain to load-bearing-type, cementing-type and pore-filling-type gas hydrate, respectively.

When gas hydrate is of the pore-filling type, it does not affect the initial porosity ϕ ; therefore, the apparent porosity ϕ_{as} (Fig. 3) equals the initial porosity ϕ , $\phi_{as} = \phi$. Conversely, when the gas hydrate is of the load-bearing type, or contact-cementing type, or envelope-cementing type, it decreases the initial porosity ϕ ; therefore, the apparent porosity is given by $\phi_{as} = \phi(1-S_h)$, where S_h is the gas-hydrate saturation.

(1) When the gas hydrate is of the pore-filling type, we apply the Voigt-Reuss-Hill (V-R-H) model to calculate the effective bulk modulus K_s and the shear modulus μ_s of the solid phase:

$$K_{s} = \left[\sum_{i=1}^{N} f_{i} K_{i} + \left(\sum_{i=1}^{N} \frac{f_{i}}{K_{i}} \right)^{-1} \right] / 2,$$

$$\mu_{s} = \left[\sum_{i=1}^{N} f_{i} \mu_{i} + \left(\sum_{i=1}^{N} \frac{f_{i}}{\mu_{i}} \right)^{-1} \right] / 2,$$
(1)

where i represents the ith mineral constituent, N represents the total number of mineral constituents, f_i is the original volumetric fraction of the ith mineral constituent, and K_i and μ_i are the bulk modulus and shear modulus of the ith mineral constituent, respectively. The effective bulk modulus of the fluid mixture containing pore-filling-type gas hydrate can be calculated using the Reuss model:

$$K_{f-h} = \left(\frac{1 - S_g - S_h}{K_W} + \frac{S_g}{K_g} + \frac{S_h}{K_h}\right)^{-1},$$
 (2)

where S_g is the free-gas saturation, and K_w , K_g and K_h are the bulk modulus of water, free gas and gas hydrate, respectively.

When the gas hydrate is of load-bearing type, or contact-cementing type, or envelope-cementing type, the volumetric fraction of the ith mineral constituent changes from f_i to $\bar{f}_i = f_i(1-\phi)/(1-\phi_{\rm as})$. The gas hydrate is treated as a mineral constituent with a volumetric fraction $\bar{f}_h = S_h \phi/(1-\phi_{\rm as})$, and the effective bulk modulus $K_{\rm S-h}$ and shear modulus $\mu_{\rm S-h}$ of the solid mixture containing load-bearing-type or cementing-type gas hydrate can be calculated using the V-R-H model:



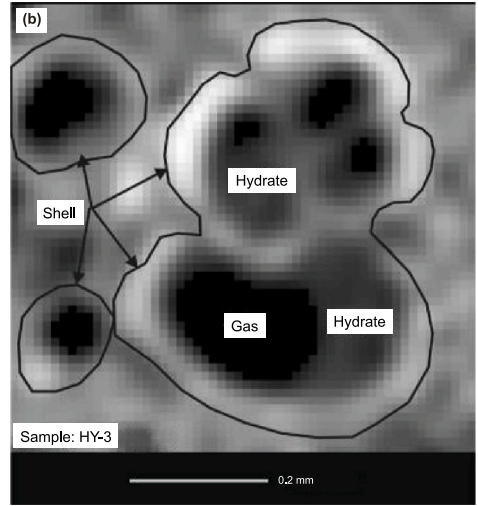


Fig. 2. (a) Natural gas hydrate sample HY-3 from SH-7 well (20%—48% hydrate saturation) in Shenhu area and (b) gas hydrate and free gas in sample HY-3 (Liu et al., 2017).

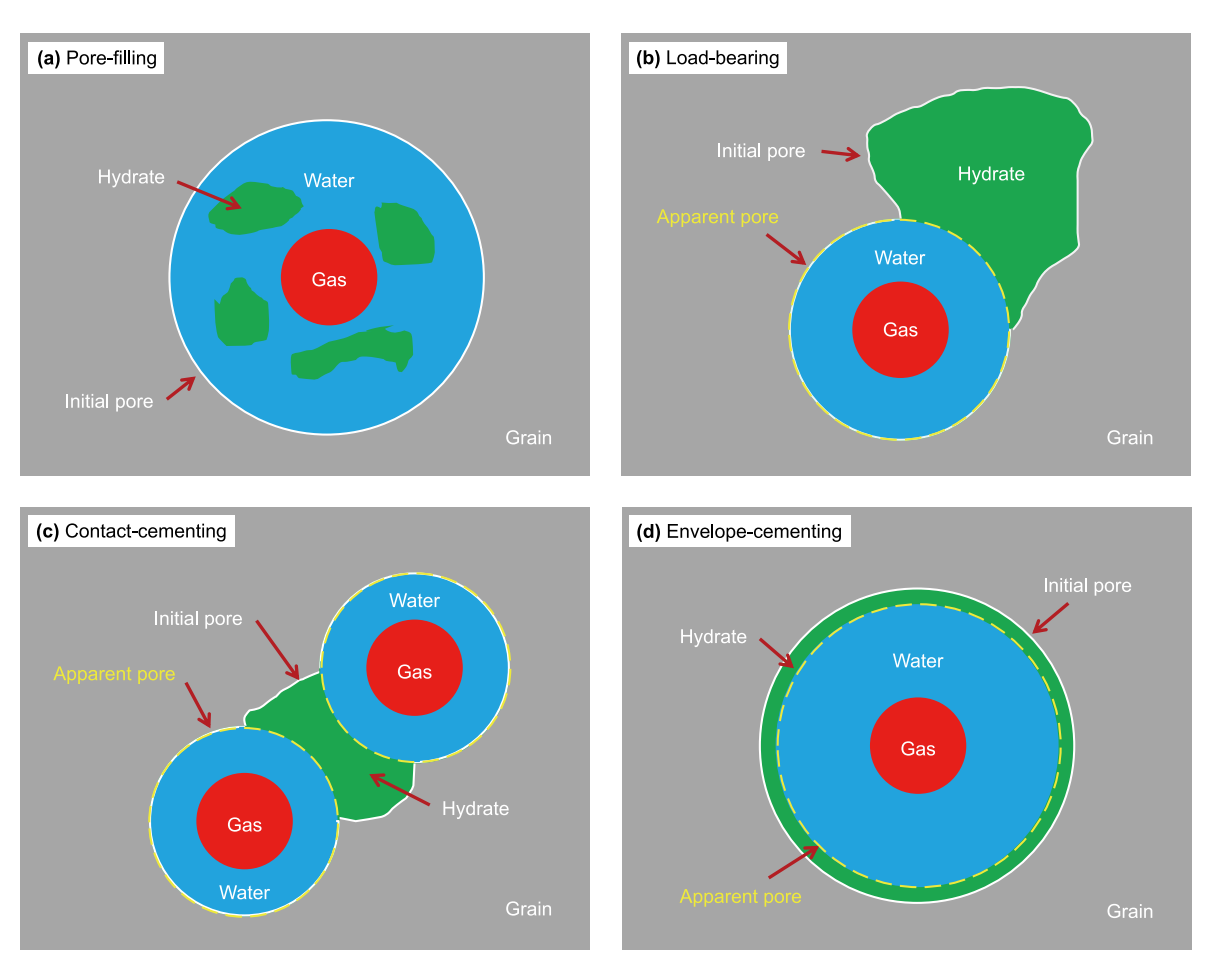


Fig. 3. Gas-hydrate occurrence states commonly used in rock physics investigation: (a) pore-filling type, (b) load-bearing type, (c) contact-cementing type and (d) envelope-cementing type.

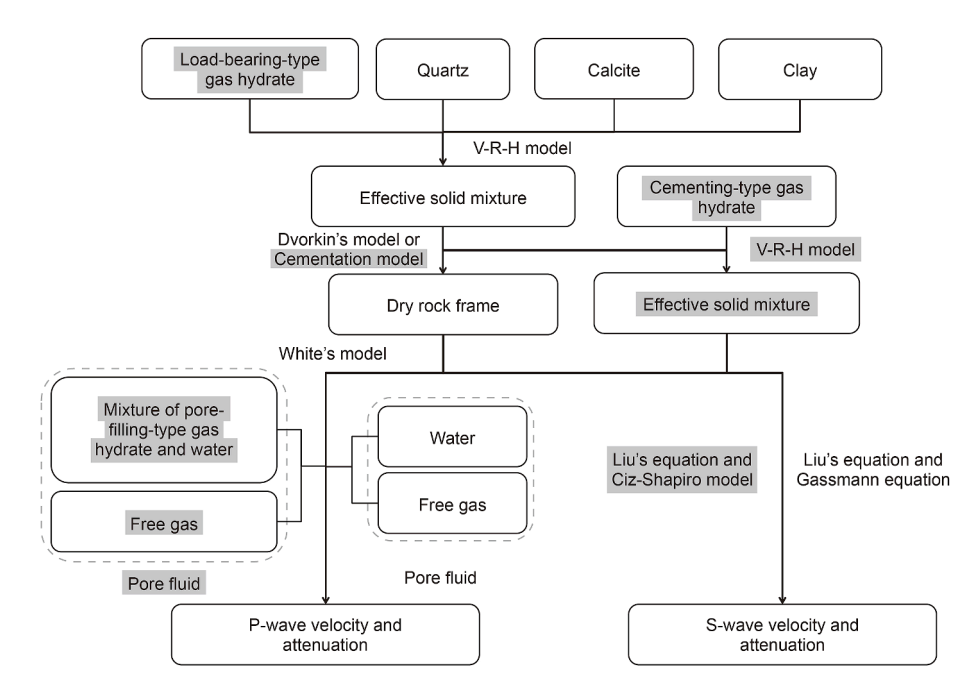


Fig. 4. The workflow of the rock physics modeling for gas hydrate-bearing formations.

$$K_{s-h} = \left[\left(\sum_{i=1}^{N} \overline{f}_{i} K_{i} + \overline{f}_{h} K_{h} \right) + \left(\sum_{i=1}^{N} \frac{\overline{f}_{i}}{K_{i}} + \frac{\overline{f}_{h}}{K_{h}} \right)^{-1} \right] / 2,$$

$$\mu_{s-h} = \left[\left(\sum_{i=1}^{N} \overline{f}_{i} \mu_{i} + \overline{f}_{h} \mu_{h} \right) + \left(\sum_{i=1}^{N} \frac{\overline{f}_{i}}{\mu_{i}} + \frac{\overline{f}_{h}}{\mu_{h}} \right)^{-1} \right] / 2,$$
(3)

where μ_h is the shear modulus of the gas hydrate. Additionally, the free-gas saturation changes from S_g to the apparent free-gas saturation $\overline{S}_g = S_g \phi / \phi_{as}$, and the effective bulk modulus K_f of the fluid phase can be calculated using the Reuss model:

$$K_{\rm f} = \left(\frac{1 - \overline{S}_{\rm g}}{K_{\rm w}} + \frac{\overline{S}_{\rm g}}{K_{\rm g}}\right)^{-1}.\tag{4}$$

(2) When the gas hydrate is of the pore-filling type, we apply the Dvorkin's effective medium model (Dvorkin et al., 1999; Guo et al., 2022) to calculate the effective bulk modulus and the shear modulus of the dry-rock frame of the gas hydrate-bearing formation. First, we apply the Hertz-Mindlin contact theory to calculate the effective bulk modulus and shear modulus of the gas hydrate-bearing formation at the critical porosity:

$$K_{\text{HM}} = \left[\frac{n^2 (1 - \phi_{\text{c}})^2 \mu_{\text{s}}^2}{18\pi^2 (1 - \nu)^2} P \right]^{\frac{1}{3}},$$

$$\mu_{\text{HM}} = \frac{5 - 4\nu}{5(2 - \nu)} \left[\frac{3n^2 (1 - \phi_{\text{c}})^2 \mu_{\text{s}}^2}{2\pi^2 (1 - \nu)^2} P \right]^{\frac{1}{3}},$$
(5)

where ϕ_c is the critical porosity, n is the coordination number, the Poisson's ratio $\nu=1/2(K_{\rm S}-2\mu_{\rm S}/3)/(K_{\rm S}+\mu_{\rm S}/3)$, and the effective pressure $P=(\rho_{\rm b}-\rho_{\rm w})gD$. Additionally, the effective density of the gas hydrate-bearing formation is given by $\rho_{\rm b}=(1-\phi)\rho_{\rm S}+\phi\rho_{\rm f}$, where $\rho_{\rm S}$ is the effective density of the solid phase, $\rho_{\rm f}$ is the effective density of the fluid mixture containing pore-filling-type gas hydrate, $\rho_{\rm w}$ is the density of water, g is the gravitational acceleration, and D is the depth below the seafloor.

Next, we apply the Dvorkin's effective medium model to calculate the effective bulk modulus $K_{\rm dry_PF}$ and shear modulus $\mu_{\rm dry_PF}$ of the dry-rock frame of the gas hydrate-bearing formation containing pore-filling-type gas hydrate:

When the gas hydrate is of the load-bearing type, we continue to apply the Dvorkin's effective medium model to calculate the effective bulk modulus $K_{\text{dry_LB}}$ and the shear modulus $\mu_{\text{dry_LB}}$ of the dry-rock frame containing load-bearing-type gas hydrate. However, the effective bulk modulus and the shear modulus of the solid phase in Eqs. (5) and (6) are modified from K_{S} and μ_{S} to $K_{\text{S-h}}$ and $\mu_{\text{S-h}}$, respectively.

When the gas hydrate is of the contact-cementing type or envelope-cementing type, we apply the cementation model (Dvorkin and Nur, 1996; Pan et al., 2022; Tian et al., 2024) to calculate the effective bulk modulus $K_{\rm dry_CM}$ and the shear modulus $\mu_{\rm dry_CM}$ of the dry-rock frame containing cementing-type gas hydrate:

$$K_{\text{dry_CM}} = \frac{n(1 - \phi)}{6} \left(K_{\text{h}} + \frac{4\mu_{\text{h}}}{3} \right) S_{n},$$

$$\mu_{\text{dry_CM}} = \frac{3K_{\text{dry_CM}}}{5} + \frac{3n(1 - \phi)\mu_{\text{h}}S_{\tau}}{20},$$
(7)

where the parameters S_n and S_τ satisfy:

$$\begin{split} S_n = & A_n(\Lambda_n)\alpha^2 + B_n(\Lambda_n)\alpha + C_n(\Lambda_n), \\ A_n(\Lambda_n) = & -0.024153\Lambda_n^{-1.3646}, \\ B_n(\Lambda_n) = & 0.20405\Lambda_n^{-0.89008}, \\ C_n(\Lambda_n) = & 0.00024649\Lambda_n^{-1.9846}, \\ S_\tau = & A_\tau(\Lambda_\tau, \nu)\alpha^2 + B_\tau(\Lambda_\tau, \nu)\alpha + C_\tau(\Lambda_\tau, \nu), \\ A_\tau(\Lambda_\tau, \nu) = & -10^{-2}\left(2.26\nu^2 + 2.07\nu + 2.3\right)\Lambda_\tau^{0.079\nu^2 + 0.1754\nu - 1.342}, \\ B_\tau(\Lambda_\tau, \nu) = & \left(0.0573\nu^2 + 0.0937\nu + 0.202\right)\Lambda_\tau^{0.0274\nu^2 + 0.0529\nu - 0.8765}, \\ C_\tau(\Lambda_\tau, \nu) = & 10^{-4}\left(9.654\nu^2 + 4.945\nu + 3.1\right)\Lambda_\tau^{0.01867\nu^2 + 0.4011\nu - 1.8186}. \end{split}$$

where

$$\begin{split} & \Lambda_n = \frac{2\mu_{\rm h}(1-\nu)(1-\nu_{\rm h})}{\pi\mu_{\rm s}(1-2\nu_{\rm h})}, \\ & \Lambda_{\tau} = \frac{\mu_{\rm h}}{\pi\mu_{\rm c}}. \end{split} \tag{9}$$

where ν is the Poisson's ratio of the solid phase, ν_h is the Poisson's ratio of the gas hydrate, and α is the ratio of the gas-hydrate

$$K_{\text{dry_PF}} = \begin{cases} \left[\frac{\phi/\phi_{\text{c}}}{K_{\text{HM}} + \frac{4}{3}\mu_{\text{HM}}} + \frac{1 - \phi/\phi_{\text{c}}}{K_{\text{s}} + \frac{4}{3}\mu_{\text{HM}}} \right]^{-1} - \frac{4}{3}\mu_{\text{HM}}, \ \phi < \phi_{\text{c}} \\ \left[\frac{(1 - \phi)/(1 - \phi_{\text{c}})}{K_{\text{HM}} + \frac{4}{3}\mu_{\text{HM}}} + \frac{(\phi - \phi_{\text{c}})/(1 - \phi_{\text{c}})}{\frac{4}{3}\mu_{\text{HM}}} \right]^{-1} - \frac{4}{3}\mu_{\text{HM}}, \ \phi \ge \phi_{\text{c}} \end{cases} ,$$

$$\mu_{\text{dry_PF}} = \begin{cases} \left[\frac{\phi/\phi_{\text{c}}}{\mu_{\text{HM}} + Z} + \frac{1 - \phi/\phi_{\text{c}}}{\mu_{\text{s}} + Z} \right]^{-1} - Z, \phi < \phi_{\text{c}} \\ \left[\frac{(1 - \phi)/(1 - \phi_{\text{c}})}{\mu_{\text{HM}} + Z} + \frac{(\phi - \phi_{\text{c}})/(1 - \phi_{\text{c}})}{Z} \right]^{-1} - Z, \phi \ge \phi_{\text{c}} \end{cases} ,$$

$$Z = \frac{\mu_{\text{HM}}}{6} \left(\frac{9K_{\text{HM}} + 8\mu_{\text{HM}}}{K_{\text{HM}} + 2\mu_{\text{HM}}} \right),$$

$$(6)$$

contact radius to the grain radius. If the gas hydrate deposits at the contact of grains, then $\alpha = 2[S_h\phi/(3n(1-\phi))]^{0.25}$; if the gas hydrate coats each grain evenly, then $\alpha = [2S_h\phi/(3(1-\phi))]^{0.5}$.

(3) We apply White's model (White, 1975; Li, 2015) to analyze the velocity dispersion and attenuation properties of the gas hydrate-bearing formations in the Shenhu area. This mesoscale model operates at a scale larger than that of individual grains but smaller than the wavelength scale. It considers a porous medium containing two types of immiscible fluids: water and gas. The attenuation mechanism of the White's model is wave-induced fluid flow, which is commonly employed to model fluid-induced velocity dispersion and attenuation in reservoir rocks. However, the P-wave velocity of White's model at zero frequency is higher than the lower limit of Biot-Gassmann-Wood theory. Therefore, we use the White's model incorporating Dutta-Odé correction to analyze the velocity dispersion and attenuation, and the P-wave velocity at zero frequency aligns well with the lower limit of the Biot-Gassmann-Wood theory.

We first assume the saturations of gas and water (or the mixture containing water and pore-filling-type gas hydrate) as S_1 and S_2 , respectively:

$$S_1 = \frac{a^3}{b^3}, S_2 = 1 - S_1, \tag{10}$$

where *a* and *b* are the radius of the free-gas pocket and the water pocket, respectively.

Additionally, gas-hydrate occurrence states influence rock parameters. When the gas hydrate is of the pore-filling type, we treat the mixture of water and pore-filling-type gas hydrate in the pores as one fluid phase, with free gas as the other. The effective bulk modulus $K_{\text{W-h}}$ of the fluid mixture containing water and pore-filling-type gas hydrate is calculated using the Reuss model:

$$K_{w-h} = \left[\frac{S_h}{K_h} + \frac{1 - S_h - S_g}{K_w}\right]^{-1},$$
 (11)

and the effective density $\rho_{\text{W-h}}$ of the fluid mixture containing water and pore-filling-type gas hydrate is calculated using Wood's formula:

$$\rho_{W-h} = S_h \rho_h + (1 - S_h - S_g) \rho_W, \tag{12}$$

however, when the pore-filling-type gas-hydrate saturation is 0%, the effective bulk modulus $K_{\text{W-h}}$ and density $\rho_{\text{W-h}}$ of the fluid mixture are equivalent to the bulk modulus and density of water:

$$K_{W-h} = K_W, \rho_{W-h} = \rho_W,$$
 (13)

When gas hydrate is of the load-bearing type, or contact-cementing type, or envelope-cementing type, the pore space contains only water and free gas. Consequently, water constitutes one fluid phase, while free gas represents the other.

Gas-hydrate occurrence state also influences the permeability of gas hydrate-bearing formations. Assuming uniform permeability across different regions, we utilize the parallel capillary model (Kleinberg et al., 2003; Ren et al., 2020) to determine the effective permeability of the gas hydrate-bearing formation. This model is particularly suitable for high-porosity gas hydrate-bearing formations, as it describes the permeability of a porous medium composed of a bundle of straight, parallel cylindrical capillaries.

When the gas hydrate is of the pore-filling type, it occupies the center of the cylindrical pores, leaving a circular flow path for water. The effective permeability κ' of the gas hydrate-bearing formation is given by

$$\kappa' = \kappa \left[1 - S_h^2 + 2(1 - S_h)^2 / \ln S_h \right],$$
 (14)

where κ is the initial permeability of the formation without gas hydrate. When the gas hydrate is of the load-bearing type, or contact-cementing type, or envelope-cementing type, we assume that the gas hydrate is uniformly coated on the walls of each capillary. The effective permeability κ' of the gas hydrate-bearing formation is given by

$$\kappa' = \kappa (1 - S_h)^2, \tag{15}$$

Then, the frequency-dependent dynamic bulk modulus $K_{\text{sat}}(\omega)$ of the gas hydrate-bearing formation is given by

$$K_{\text{sat}}(\omega) = \frac{K_{\text{GH}}}{1 - WK_{\text{CH}}},\tag{16}$$

where $K_{\rm GH}$ is the bulk modulus of the composite, including fluid and matrix, at the high-frequency limit (Picotti et al., 2010), and W is a weighting parameter. The details of $K_{\rm GH}$ and W are introduced in the Appendix A.

When the gas hydrate is of the pore-filling type, according to Wu et al. (2024), the shear modulus μ_{sat} of the gas hydrate-bearing formation is given by

$$\mu_{\text{sat}} = \left[\mu_{\text{dry_PF}}^{-1} - \frac{\left(\mu_{\text{dry_PF}}^{-1} - \mu_{\text{s}}^{-1}\right)^{2}}{\phi\left(\mu_{\text{f-h}}^{-1} - \mu_{\text{s}}^{-1}\right) + \left(\mu_{\text{dry_PF}}^{-1} - \mu_{\text{s}}^{-1}\right)} \right]^{-1}, \quad (17)$$

where μ_{f-h} is the shear modulus of the effective pore filler. According to Wu et al. (2024), we apply the modified V-R-H model to calculate the shear modulus μ_{f-h} of the effective pore filler:

$$\mu_{f-h} = \left[S_{h} \mu_{h} + S_{g} \mu_{g} + (1 - S_{h} - S_{g}) \mu_{w} \right] \beta$$

$$+ \left[\frac{S_{h}}{\mu_{h}} + \frac{S_{g}}{\mu_{g}} + \frac{1 - S_{h} - S_{g}}{\mu_{w}} \right]^{-1} (1 - \beta), \tag{18}$$

where the weight coefficient $\beta = 0.1$. Note that the shear modulus of gas and water cannot be zero when they are placed in the denominator position, we use a very small value 10^{-10} in the modeling

When the gas hydrate is of the load-bearing type, according to Mavko et al. (2009), the shear modulus μ_{sat} of the gas hydrate-bearing formation is given by

$$\mu_{\mathsf{sat}} = \mu_{\mathsf{dry_LB}},\tag{19}$$

When the gas hydrate is of the contact-cementing type or envelope-cementing type, according to Mavko et al. (2009), the shear modulus μ_{sat} of the gas hydrate-bearing formation is given by

$$\mu_{\text{sat}} = \mu_{\text{drv_CM}},\tag{20}$$

Then, the complex P-wave velocity is given by

$$V = \sqrt{\frac{K_{\text{sat}}(\omega) + 4\mu_{\text{sat}}/3}{\rho_{\text{b}}}},\tag{21}$$

The P-wave phase velocity and attenuation are given by

$$V_{\rm P} = \frac{1}{{\rm Re}(1/V)}, \ Q_{\rm P}^{-1} = \frac{{\rm Im}(V^2)}{{\rm Re}(V^2)},$$
 (22)

According to Liu et al. (2011), the S-wave velocity and attenuation are given by

$$V_{S} = \sqrt{\frac{\mu_{\text{sat}}}{\rho_{\text{b}}} \frac{\gamma_{2}^{2} + (\gamma_{3}/\omega)^{2}}{\gamma_{2}^{2} - \gamma_{1}^{2}\gamma_{2} + (\gamma_{3}/\omega)^{2}}}, \ Q_{S}^{-1} = \frac{(\gamma_{3}/\omega)\gamma_{1}^{2}}{\gamma_{2}^{2} - \gamma_{1}^{2}\gamma_{2} + (\gamma_{3}/\omega)^{2}}$$
(23)

where $\gamma_1 = \rho_f/\rho_b$, $\gamma_2 = M/\rho_b$, and $\gamma_3 = (\eta/\kappa')/\rho_b$, and $M = K_s[1-K_{dry}/K_s+\phi(K_s/K_f-1)]^{-1}$, and ρ_f is the effective density of the fluid phase, and η is the effective viscosity of the fluid phase. When the gas hydrate is of the pore-filling type, $\rho_f = (1-S_h-S_g)\rho_W + S_h\rho_h + S_g\rho_g$ and $\eta = (1-S_h-S_g)\eta_W + S_g\eta_g$; when the gas hydrate is of the loadbearing type, or contact-cementing type, or envelope-cementing type, $\rho_f = (1-\overline{S}_g)\rho_W + \overline{S}_g\rho_g$ and $\eta = (1-\overline{S}_g)\eta_W + \overline{S}_g\eta_g$.

3.3. Velocity dispersion and attenuation properties of gas hydratebearing formations

First, we consider four types of gas-hydrate occurrence states. We then apply four rock physics models to estimate the effective bulk modulus and shear modulus of the dry-rock frame of formations containing four types of gas hydrate. Subsequently, we apply White's model to analyze the velocity dispersion and attenuation properties of these formations. The input parameters are detailed in Table 1. We consider free-gas saturation of 1%, 5% and 20%, and assume the initial porosity to be 43%, and the volume percentage of quartz, calcite and clay to be 45%, 20% and 35%, respectively. We also assume the depth below the seafloor *D* to be 220 m. These parameters are adopted based on the real logs shown in Fig. 1. Finally, we calibrate the rock physics model using well log data and examine the sensitivity of P- and S-wave velocities, as well as attenuation properties, to frequency, gas-hydrate saturation, and free-gas saturation.

Table 1
Input parameters for rock physics modeling (Helgerud et al., 1999; Mavko et al., 2009; Best et al., 2013; Li and Liu, 2017; Li et al., 2018; Meng et al., 2020; Liu, 2022; Wu et al., 2023)

Parameters and units	Value
Quartz bulk modulus, GPa	36.6
Calcite bulk modulus, GPa	76.8
Clay bulk modulus, GPa	20.9
Quartz shear modulus, GPa	45
Calcite shear modulus, GPa	32
Clay shear modulus, GPa	6.85
Hydrate bulk modulus, GPa	7.9
Gas bulk modulus, GPa	0.4
Water bulk modulus, GPa	2.5
Hydrate shear modulus, GPa	3.3
Quartz density, kg/m ³	2650
Calcite density, kg/m ³	2710
Clay density, kg/m ³	2580
Hydrate density, kg/m ³	900
Water density, kg/m ³	1032
Gas density, kg/m³	230
The viscosity of water, Pa·s	0.001
The viscosity of gas, Pa·s	0.00002
Critical porosity, %	36
Grain coordination number	8
Outer radius of White's spherical model, m	0.01 and 0.05
Permeability, mD	1.5

Fig. 5 illustrates significant dispersion in P-wave velocity, with the transition zone occurring within the seismic frequency range. For pore-filling-type gas hydrate, P-wave attenuation decreases as frequency increases. In contrast, for load-bearing, contact-cementing, and envelope-cementing types, P-wave attenuation initially increases and then decreases as frequency increases, with the peak attenuation occurring within the seismic frequency range. Additionally, as gas-hydrate saturation increases, the amplitude of the relationship between P-wave attenuation and frequency for these four types of gas hydrate-bearing formations changes nonlinearly.

3.4. Relationship between velocity and attenuation properties and gas-hydrate saturation

Fig. 6 illustrates that for pore-filling-type and load-bearingtype gas hydrate, the estimated P- and S-wave velocities agree with well logs very consistently. In contrast, for contactcementing-type and envelope-cementing-type gas hydrate, the estimated velocities are higher than those recorded in the well logs. This indicates that the two rock physics models used in this study—the pore-filling-type model and the load-bearing-type model, which combine White's model and Dvorkin's effective medium model—are both reliable and more suitable for simulating gas hydrate-bearing formations in the Shenhu area of the South China Sea. However, it's well worth mentioning that when gas-hydrate saturation exceeds 40%, the S-wave velocity of loadbearing-type gas hydrate aligns more closely with the real data compared to pore-filling-type gas hydrate. Note that the modelled P- and S-wave velocities can be significantly lower than the measured velocities when gas-hydrate saturation is close to zero. Therefore, we change the free-gas saturation to make the modelled velocity to align well with the measured velocity.

Fig. 7 illustrates the P-wave attenuation for the four gas-hydrate occurrence states at a frequency of 40 Hz, which corresponds to the dominant frequency of the extracted wavelet from the gas hydrate-bearing formation region in the pre-stack seismic data. It can be observed that for pore-filling-type, contact-cementing-type, and envelope-cementing-type gas hydrate, P-wave attenuation initially increases and then decreases as gas-hydrate saturation increases, with peak attenuation occurring at 0%–10% gas-hydrate saturation. For the load-bearing type, P-wave attenuation first decreases, then slightly increases, and subsequently decreases again as gas-hydrate saturation increases, the amplitude of the relationship between the P-wave attenuation and gas-hydrate saturation amplifies within the 0%–60% gas-hydrate saturation range.

4. Seismic forward modeling for gas hydrate-bearing formations

We apply the propagator matrix method (Carcione, 2001; Guo et al., 2016) to calculate the reflection and transmission coefficients for a thin inter-bedded model (Fig. 8). This method accounts for the effects of thin inter-bedded structures, as well as the velocity dispersion and attenuation properties of hydrocarbon-bearing formation, on seismic wave propagation.

The matrix equation for this method is expressed as

$$(\mathbf{A}_{1} - \mathbf{B}\mathbf{A}_{2})\mathbf{r} = -\mathbf{i}_{P}, \mathbf{r} = [R_{PP}, R_{PS}, T_{PP}, T_{PS}]^{T},$$
(24)

where \mathbf{A}_1 , \mathbf{A}_2 and \mathbf{B} represent the propagator matrices of the upper, lower, and middle thin layer, respectively; \mathbf{r} is the vector of reflection and transmission coefficients; \mathbf{i}_P is the incidence vector; R_{PP} is the reflection coefficient for P-wave incidence and P-wave

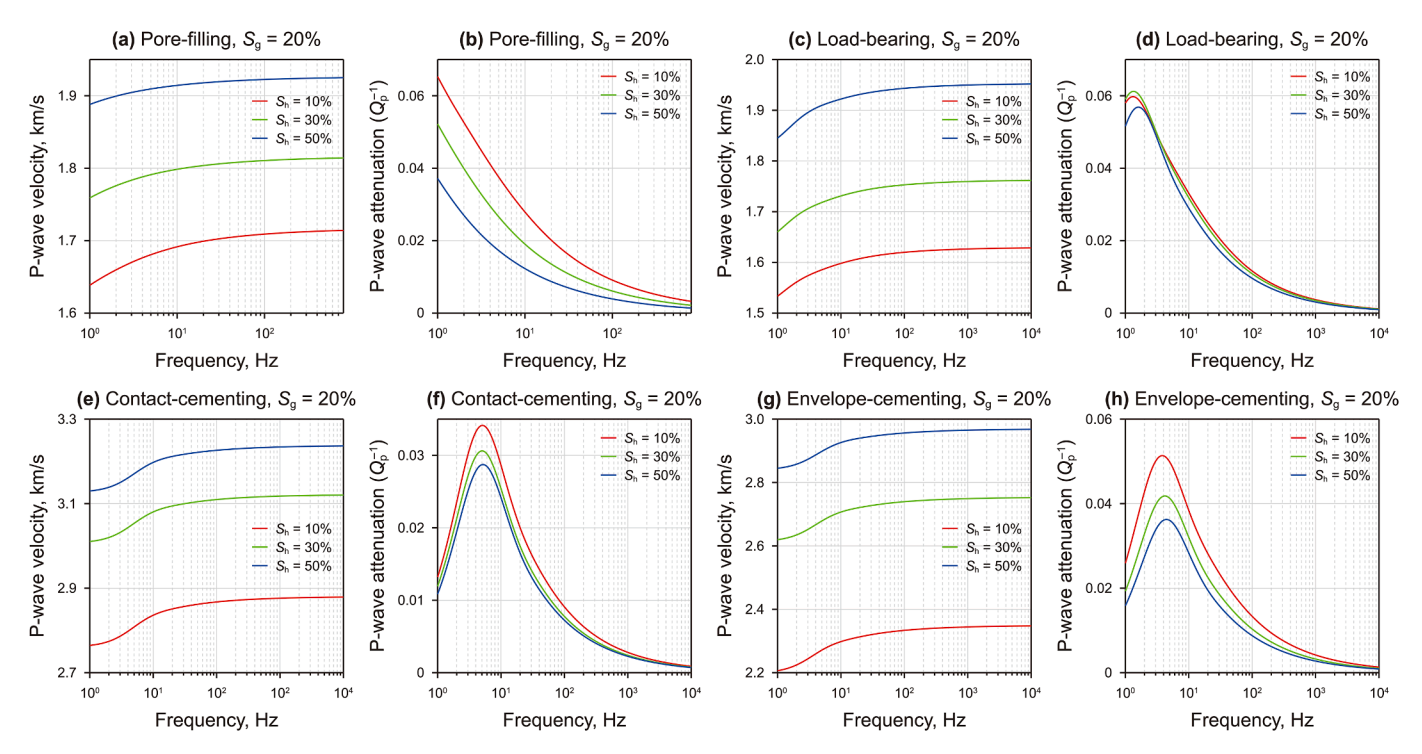


Fig. 5. Modelled P-wave velocity and attenuation versus frequency for formations containing different types of gas hydrate using Dvorkin's, cementation and White's model: (a) and (b) pore-filling type, (c) and (d) load-bearing type, (e) and (f) contact-cementing type, and (g) and (h) envelope-cementing type.

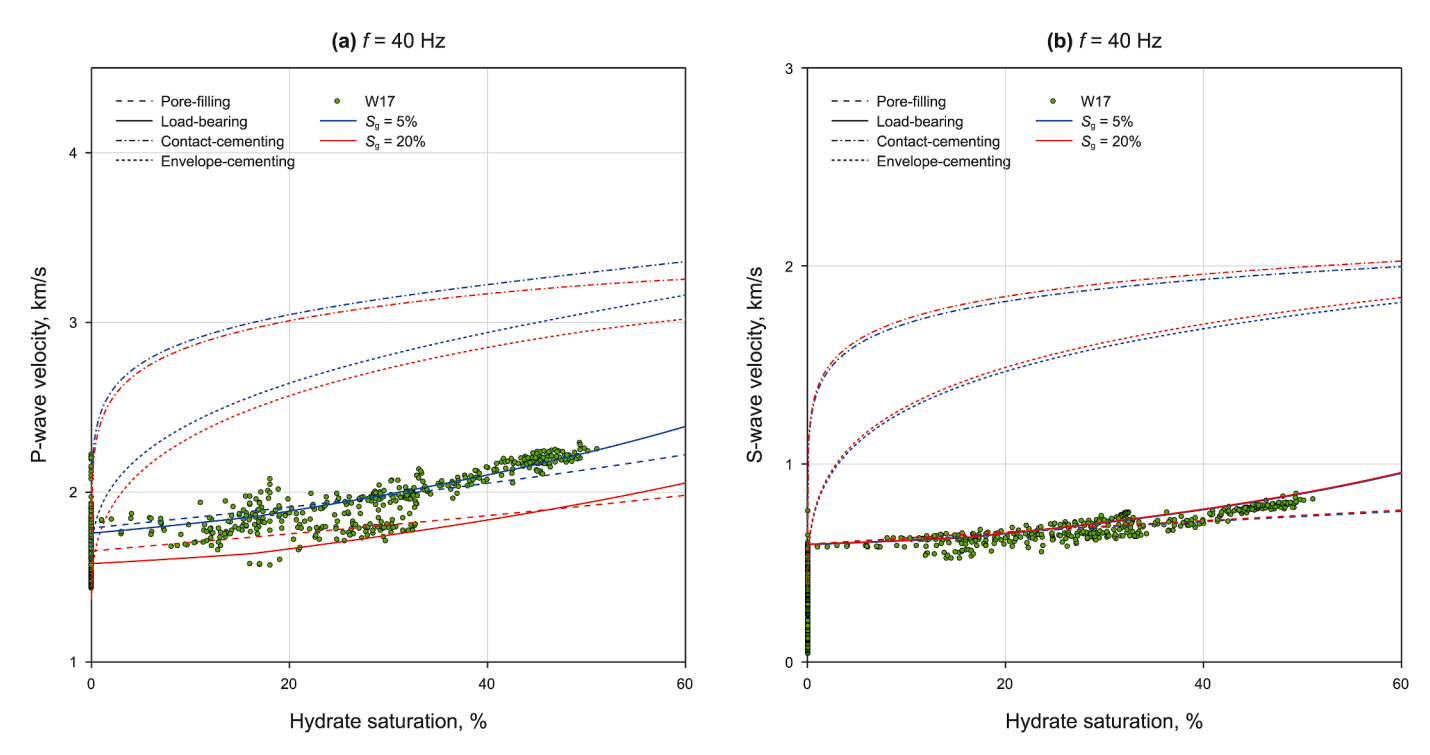


Fig. 6. Modelled (a) P-wave velocity and (b) S-wave velocity versus gas-hydrate saturation for formations containing different types of gas hydrate using Dvorkin's, cementation and White's model at frequency (f) 40 Hz.

reflection; $R_{\rm PS}$ is the reflection coefficient for P-wave incidence and S-wave reflection, $T_{\rm PP}$ is the transmission coefficient for P-wave incidence and P-wave transmission; and $T_{\rm PS}$ is the transmission coefficient for P-wave incidence and S-wave reflection.

Next, we apply the inverse Fourier transform to obtain the synthetic angle gather incorporating attenuation:

$$S(t,\theta) = \frac{1}{2\pi} \int_{-\infty}^{\infty} R_{PP}(\omega,\theta) W(\omega) \exp(i\omega t) d\omega.$$
 (25)

where $R_{PP}(\omega,\theta)$ is the frequency-domain reflection coefficient, W (ω) is the spectrum of the wavelet after the Fourier transform, and

the wavelet is extracted from the gas hydrate-bearing formation region in the pre-stack seismic data.

We apply our preferred rock physics model, combining White's model and the Dvorkin's effective medium model, to estimate the attenuation ($100/Q_p$) logs, as shown in Fig. 9(b) and (c). Fig. 9(b) presents the estimated attenuation logs for the pore-filling-type gas hydrate, while Fig. 9(c) shows those for the load-bearing-type gas hydrate. The results indicate that the estimated P-wave attenuation logs for gas hydrate-bearing formations are reasonable. The estimated S-wave attenuation approaches zero, as fluids do not influence S-wave propagation. Therefore, we assume Q_s equals Q_p (Kamei, 2012; Jafargandomi and Curtis, 2013).

Additionally, the attenuation for the load-bearing-type gas hydrate is slightly higher than that for the pore-filling-type gas hydrate, suggesting that the load-bearing-type gas hydrate decreases porosity and increases free-gas saturation, thereby increasing attenuation. Variations in gas-hydrate and free-gas saturation also significantly impact the estimated attenuation for both the pore-filling and load-bearing types, as illustrated in Fig. 7. Furthermore, the highest estimated attenuation occurs in the mixed formations, where the free-gas saturation is maximal.

In the gas hydrate-bearing formations, when the gas hydrate is of the load-bearing type, the estimated P- and S-wave velocities agree with the well logs very well. However, for the pore-filling

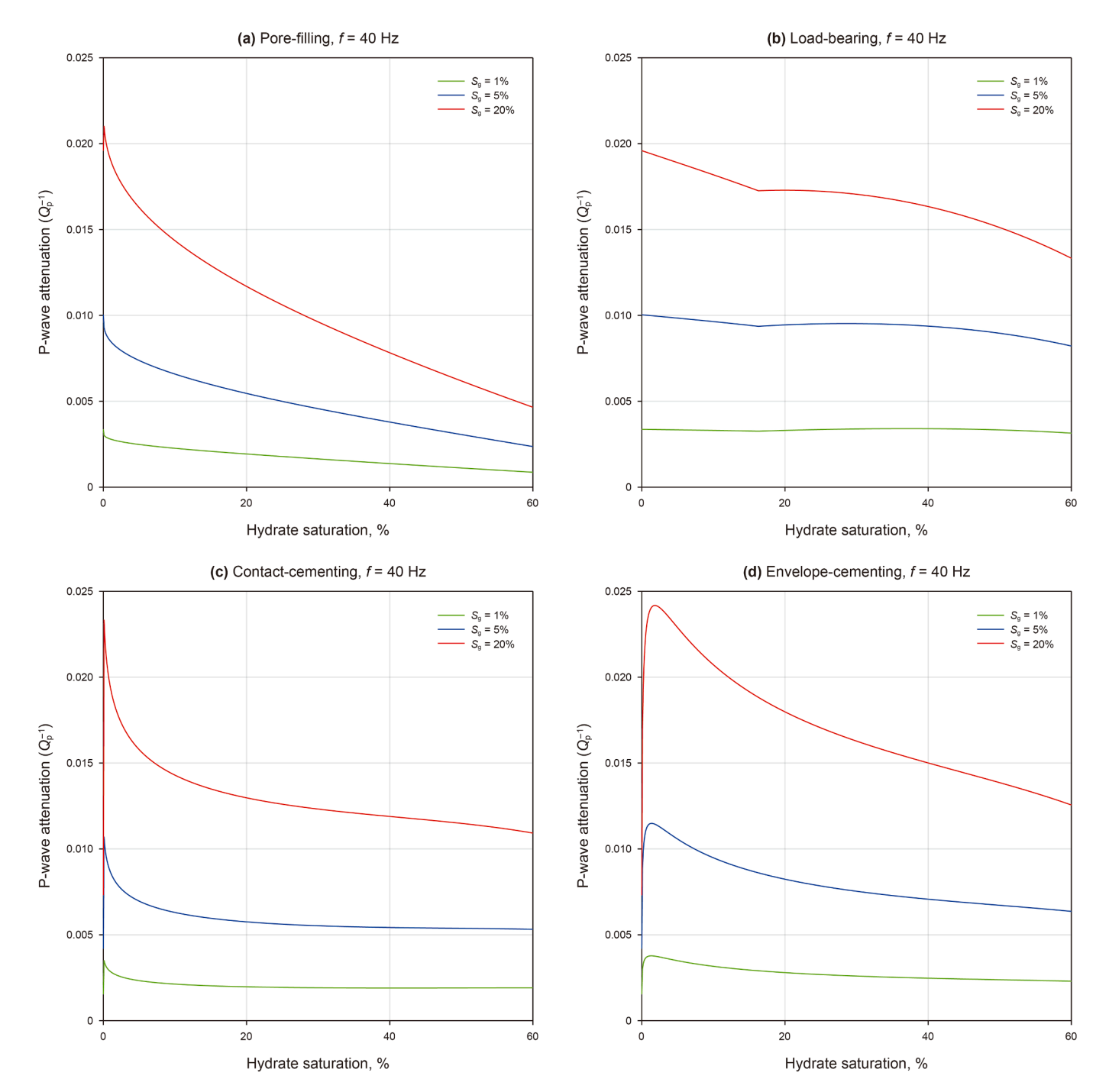


Fig. 7. Modelled P-wave attenuation versus gas-hydrate saturation for formations containing different types of gas hydrate using Dvorkin's, cementation and White's model: (a) pore-filling type, (b) load-bearing type, (c) contact-cementing type and (d) envelope-cementing type at frequency 40 Hz.

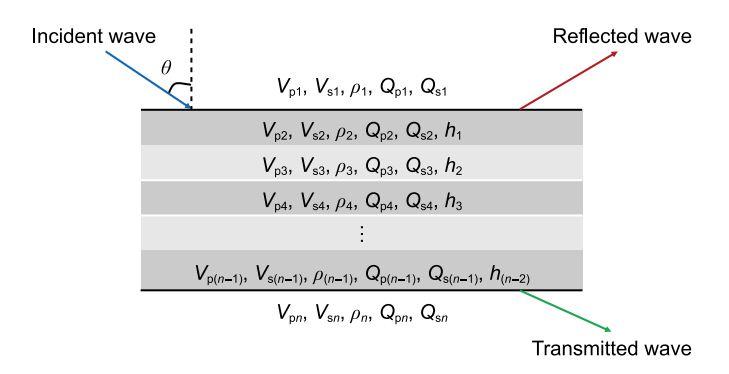


Fig. 8. Diagram of the thin inter-bedded model.

type, the estimated velocities are lower than the real velocities, suggesting that the gas hydrate in these formations is more likely to be of the load-bearing type. In the mixed formations, regardless of whether the gas hydrate is of the pore-filling or load-bearing type, the estimated P- and S-wave velocities match the well logs, implying that gas hydrate can be either type in these formations. This also suggests that variations in depth, pressure, and temperature may influence the gas-hydrate occurrence state.

Compared to the well tie in Fig. 1, Fig. 10 presents the synthetic angle gathers incorporating attenuation near a well via the propagator matrix method for both the pore-filling-type and load-bearing-type gas hydrate-bearing formations. The well tie shows a generally improved match; for instance, the AVO characteristic of the event below 1960 ms (1498 m) in the synthetic angle gathers generated using the propagator matrix method is better than that in the synthetic angle gather generated using the convolution method. Furthermore, the amplitudes of the two events below 1980 ms (1516 m) and 2000 ms (1534 m) in the synthetic angle gather generated using the convolution method are obviously strong, while the two events in the synthetic angle gathers

generated using the propagator matrix method are more balanced with upper events because of dispersion and attenuation, which is more consistent with that in the real seismic angle gather near a well. Additionally, frequency-dependent AVO and attenuation characteristics in the gas hydrate-bearing formations can also be observed in the synthetic angle gathers generated using the propagator matrix method, which are absent in synthetic angle gather generated using the convolution method. However, the synthetic angle gathers incorporating attenuation for pore-filling-type and load-bearing-type gas hydrate are quite similar, making it challenging to differentiate the gas-hydrate occurrence state using seismic data.

5. Discussions

We have adopted a rock physics model, which integrates White's model and Dvorkin's effective medium model, to analyze the velocity dispersion and attenuation properties of gas hydrate-bearing formations in the Shenhu area. The estimated relationship between velocity and gas-hydrate saturation agrees with well logs very well, confirming the reliability of our rock physics modeling. However, one limitation is that White's model, which focuses on wave-induced fluid flow, results in zero estimated S-wave attenuation, making it challenging to accurately estimate S-wave attenuation for gas hydrate-bearing formations.

Another issue is that, both dispersion and mixed hydrate types can influence velocity. Specifically, the presence of cementing-type gas hydrate may significantly increase velocity. This study primarily focuses on analyzing the velocity dispersion associated with pore-filling and load-bearing types. The potential influence of mixed hydrate types will be explored in future research.

Besides, the estimated attenuation for load-bearing-type gas hydrate-bearing formations is higher than that for pore-filling-type gas hydrate-bearing formations, suggesting that load-bearing-type gas hydrate decreases porosity, increases free-gas saturation, and

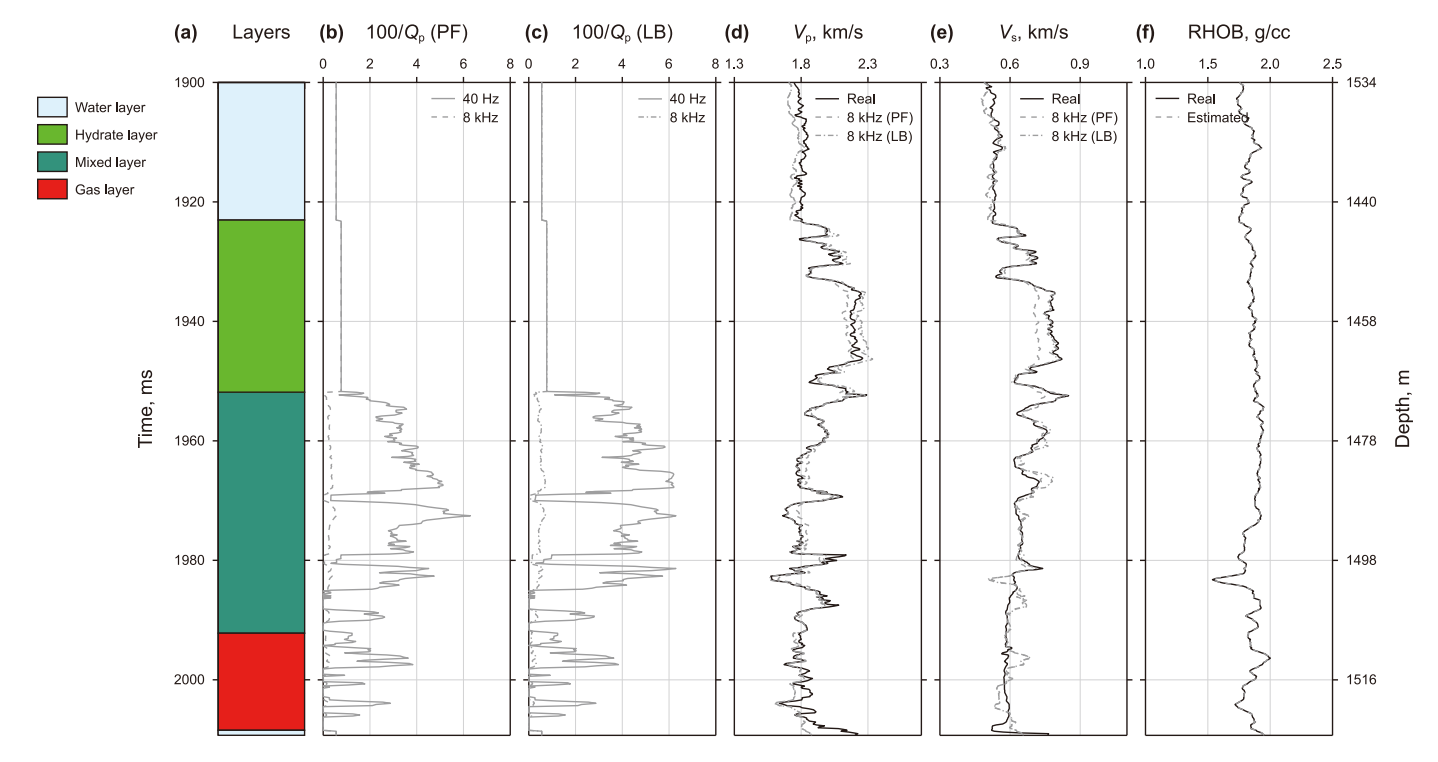


Fig. 9. (a) Geological interpretation of well W17, and logs of well W17, (b) estimated attenuation logs of pore-filling-type gas hydrate-bearing formations, (c) estimated attenuation logs of load-bearing-type gas hydrate-bearing formations, (d) real and estimated P-wave velocity, (e) real and estimated S-wave velocity, (f) density. "PF" and "LB" in (b), (c), (d) and (e) represent pore-filling and load-bearing type, respectively.

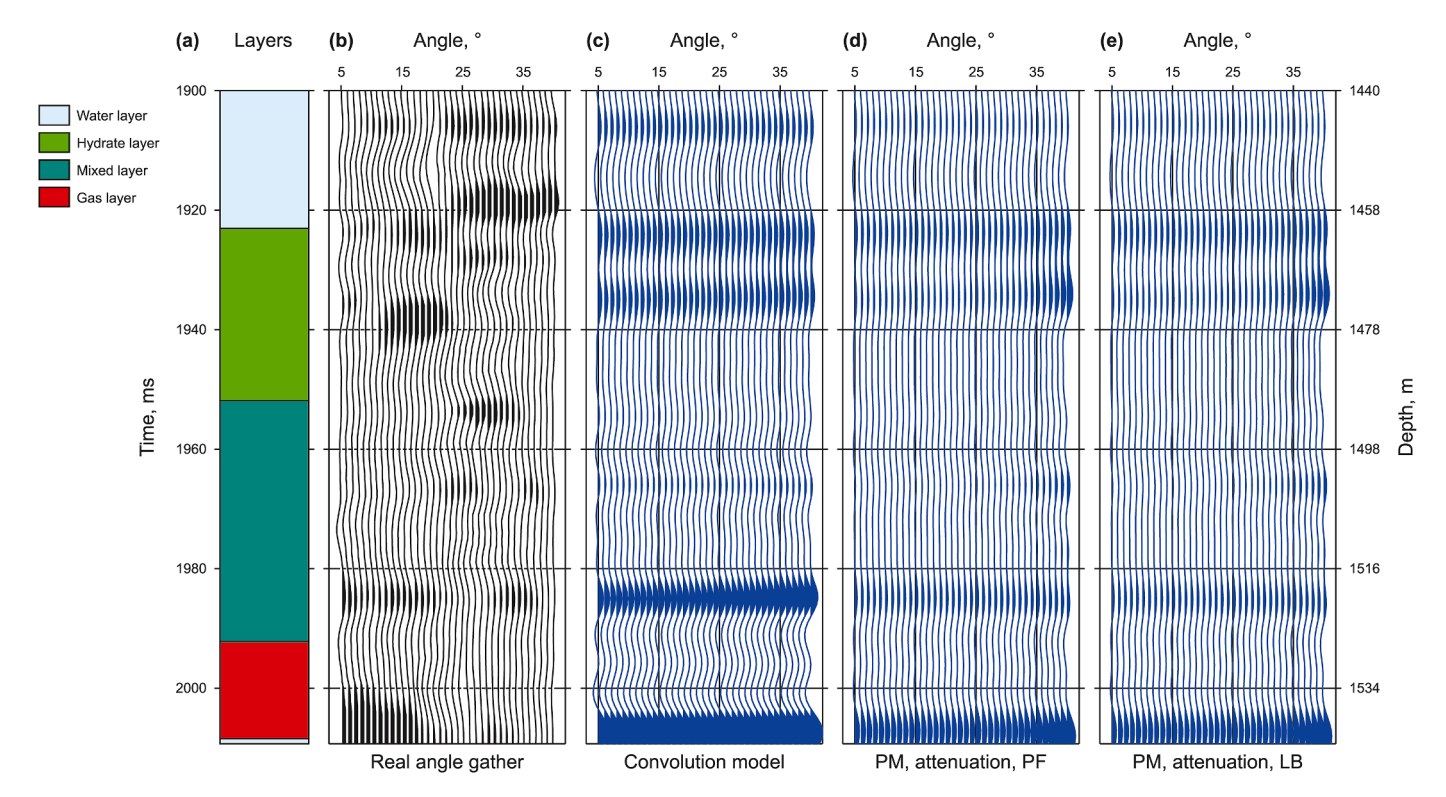


Fig. 10. (a) Geological interpretation of well W17. (b) Real seismic angle gather near a well, (c) synthetic angle gather generated using the convolution method, (d) synthetic angle gather incorporating attenuation via propagator matrix method for pore-filling-type gas hydrate-bearing formations, (e) same as (d) but for load-bearing-type gas hydrate-bearing formations. "PM" in (d) and (e) represents propagator matrix method. "PF" and "LB" in (d) and (e) represent pore-filling type and load-bearing type, respectively.

subsequently enhances attenuation. Variations in gas-hydrate and free-gas saturations also significantly influence the estimated attenuation for both pore-filling-type and load-bearing-type gas hydrate-bearing formations, as illustrated in Fig. 7.

We conducted seismic forward modeling by integrating the propagator matrix method with attenuation logs derived from our rock physics modeling. This approach allows us to obtain synthetic angle gathers incorporating attenuation near a well for formations containing different types of gas hydrate. The well tie shows an improved match between synthetic and real data compared with the convolution model, highlighting the advantages of our rock physics and seismic forward modeling approach.

Nevertheless, we note that the AVO characteristics of the events in the synthetic angle gathers incorporating attenuation differ from those in the real seismic angle gather near a well slightly. This discrepancy indicates the need for more realistic model parameters or improved rock physics models to achieve highly accurate quality factor estimates, as we know, accurate P- and S-wave quality factor logs are essential for seismic forward modeling.

6. Conclusions

In this paper, we develop a rock physics model that integrates White's model with Dvorkin's effective medium model, specifically tailored for the gas hydrate-bearing formations in the Shenhu area of the South China Sea. We apply the White's model to analyze the velocity dispersion and attenuation properties of those formations based on the four types of gas-hydrate occurrence states, and find that the estimated relationship between velocity and gas-hydrate saturation matches with well logs very consistently, demonstrating the reliability of our rock physics modeling. Furthermore, we use a set of well logs to demonstrate that two types of gas-hydrate occurrence states—pore-filling type and load-bearing type—may be present in the Shenhu area.

Additionally, by combining the propagator matrix method with attenuation logs derived from our rock physics model, we generate synthetic angle gathers incorporating attenuation near a well. The well tie analysis indicates that these synthetic angle gathers match the real seismic angle gather near a well better compared to the synthetic angle gather generated using the convolution model. These findings enhance the capability for frequency-dependent AVO analysis and seismic interpretation of gas hydrate-bearing formations in the Shenhu area, contributing valuable insights to further research and exploration in this region.

CRediT authorship contribution statement

Zuo-Xiu He: Writing – review & editing, Writing – original draft. **Feng Zhang:** Writing – review & editing, Supervision, Project administration, Conceptualization. **Pin-Bo Ding:** Supervision, Data curation. **Xiang-Yang Li:** Writing – review & editing, Supervision, Conceptualization. **Hai-Feng Chen:** Resources.

Data availability statements

The data underlying this article will be shared on reasonable request to the corresponding author.

Declaration of generative AI and AI-assisted technologies in the writing process

During the preparation of this work the author(s) used ChatGPT in order to improve language and readability. After using this tool/service, the author(s) reviewed and edited the content as needed and take(s) full responsibility for the content of the publication.

Declaration of competing interest

The authors declare that they have no known competing financial interests or personal relationships that could have appeared to influence the work reported in this paper.

Acknowledgment

This work was supported by National Natural Science Foundation of China (W2431028, 42122029), SINOPEC Fundamental Research Program (P24258), CNPC Investigations on fundamental experiments and advanced theoretical methods in geophysical prospecting applications (2022DQ0604-02).

Appendix A

The patchy saturation model presents a gas-filled spherical porous medium located inside a water-filled spherical porous medium, and their radius are a and b (a < b), respectively (White, 1975). The size of spherical patches is assumed to be much larger than the size of grains and much smaller than the wavelength. The saturation of gas and water are respectively expressed as:

$$S_1 = \frac{a^3}{b^3}, S_2 = 1 - S_1, \tag{A1}$$

The dynamic bulk modulus as a function of frequency is given by

$$K_{\text{sat}}(\omega) = \frac{K_{\text{GH}}}{1 - WK_{\text{CH}}},\tag{A2}$$

According to Picotti et al. (2010), $K_{\rm GH}$ is the bulk modulus of the composite, including fluid and matrix, at the high-frequency limit:

$$K_{\rm GH} = \left(\frac{S_1}{E_{\rm G1}} + \frac{S_2}{E_{\rm G2}}\right)^{-1} - \frac{4}{3}\mu_{\rm m},$$
 (A3)

and

$$\begin{split} W &= \frac{3i \alpha \kappa_1 (R_1 - R_2)}{b^3 \omega (\eta_1 Z_1 - \eta_2 Z_2)} \left(\frac{M_1}{K_{G1}} - \frac{M_2}{K_{G2}}\right), \\ R_1 &= \frac{(K_{G1} - K_{m1})(3K_{G2} + 4\mu_{m1})}{K_{G2}(3K_{G1} + 4\mu_{m1}) + 4\mu_{m1}(K_{G1} - K_{G2})S_1}, \\ R_2 &= \frac{(K_{G2} - K_{m2})(3K_{G1} + 4\mu_{m1})}{K_{G2}(3K_{G1} + 4\mu_{m2}) + 4\mu_{m2}(K_{G1} - K_{G2})S_1}, \\ Z_1 &= \frac{1 - \exp(-2\gamma_1 a)}{(\gamma_1 a - 1) + (\gamma_1 a + 1)\exp(-2\gamma_1 a)}, \\ Z_2 &= \frac{(\gamma_2 b + 1) + (\gamma_2 b - 1)\exp[2\gamma_2 (b - a)]}{(\gamma_2 b + 1)(\gamma_2 a - 1) - (\gamma_2 b - 1)(\gamma_2 a + 1)\exp[2\gamma_2 (b - a)]}, \\ \gamma_j &= \sqrt{i\omega\eta_j \Big/ \Big(\kappa_j K_{Aj}\Big)}, \\ K_{Aj} &= \frac{K_m}{K_{Gj}} M_j, \ j = 1, 2, \\ \omega &= 2\pi f, \end{split}$$

where f is the frequency, and the subscript j=1,2 represent gas (j=1) and water (j=2), or the medium containing gas or water, respectively; κ_j and η_j are the permeability and viscosities, respectively, and E_{Gj} are given by

$$E_{Gj} = K_{Gj} + \frac{4}{3}\mu_{mj}, j = 1, 2,$$
 (A5)

where μ_{mj} are the shear modulus of the dry-rock frame, and K_{Gj} are the Gassmann bulk modulus:

$$K_{Gj} = K_{mj} + \alpha_j^2 M_j, j = 1, 2,$$
 (A6)

where K_{mj} are the bulk modulus of the dry-rock frame, and α_j are the Biot-Willis coefficient:

$$\alpha_{j} = 1 - \frac{K_{mj}}{K_{si}}, j = 1, 2,$$
 (A7)

and M_i are given by

$$M_{j} = \left(\frac{\alpha_{j} - \phi_{j}}{K_{sj}} + \frac{\phi_{j}}{K_{fj}}\right)^{-1}, j = 1, 2,$$
 (A8)

where K_{sj} are the modulus of the matrix, and K_{fj} are the bulk modulus of the fluid, ϕ_i are the porosity.

The effective density ρ_e is given by

$$\rho_{e} = (1 - \varphi)\rho_{s} + \varphi\rho_{fe}, \tag{A9}$$

where $\rho_{\rm S}$ is the density of the matrix, and the density $\rho_{\rm fe}$ of the fluid is given by

$$\rho_{\text{fe}} = S_1 \rho_{\text{g}} + S_2 \rho_{\text{W}},\tag{A10}$$

where $\rho_{\rm g}$ and $\rho_{\rm w}$ are the densities of gas and water, respectively. The complex P-wave velocity is given by

$$V = \sqrt{\frac{K_{\text{sat}}(\omega) + 4\mu_{\text{sat}}/3}{\rho_{\text{e}}}},\tag{A11}$$

The P-wave phase velocity and inverse quality factor are given by

$$V_{\rm P} = \frac{1}{\text{Re}(1/V)}, \ Q_{\rm P}^{-1} = \frac{\text{Im}(V^2)}{\text{Re}(V^2)}.$$
 (A12)

References

Bai, C.Y., Su, P.B., Su, X., et al., 2022. Characterization of the sediments in a gas hydrate reservoir in the northern South China Sea: implications for gas hydrate accumulation. Mar. Geol. 453, 106912. https://doi.org/10.1016/j.margeo.2022.106912.

Best, A.I., Priest, J.A., Clayton, C.R.I., et al., 2013. The effect of methane hydrate morphology and water saturation on seismic wave attenuation in sand under shallow sub-seafloor conditions. Earth Planet Sci. Lett. 368, 78–87. https://doi.org/10.1016/j.epsl.2013.02.033.

Carcione, J.M., 2001. Amplitude variations with offset of pressure-seal reflections. Geophysics 66 (1), 283–293. https://doi.org/10.1190/1.1444907.

Chen, Z.Y., You, C.Y., Lyu, T., et al., 2020. Numerical simulation of the depressurization production of natural gas hydrate reservoirs by vertical well patterns in the northern South China Sea. Nat. Gas. Ind. 40 (8), 177–185. https://doi.org/10.3787/j.issn.1000-0976.2020.08.015 (in Chinese).

Dai, D.Q., Liu, X.W., Li, C.H., 2018. Identifying gas hydrate occurrence state by seismic P-wave attenuation in northern South China Sea. Geosci. J. 22, 445–452. https://doi.org/10.1007/s12303-017-0064-y.

Dvorkin, J., Nur, A., 1996. Elasticity of high-porosity sandstones: theory for two North Sea data sets. Geophysics 61 (5), 1363–1370. https://doi.org/10.1190/1.1444059.

Dvorkin, J., Prasad, M., Sakai, A., et al., 1999. Elasticity of marine sediments: rock physics modeling. Geophys. Res. Lett. 26 (12), 1781–1784. https://doi.org/10.1029/1999G1900332.

Farhadian, A., Shadloo, A., Zhao, X., et al., 2023. Challenges and advantages of using environmentally friendly kinetic gas hydrate inhibitors for flow assurance application: a comprehensive review. Fuel 336, 127055. https://doi.org/ 10.1016/j.fuel.2022.127055.

(A4)

Gu, Y.H., Li, S.J., Song, Z.Y., et al., 2024. Analysis on a five-spot well for enhancing energy recovery from silty natural gas hydrate deposits in the South China Sea. Appl. Energy 376, 124237. https://doi.org/10.1016/j.apenergy.2024.124237.

- Guerin, G., Goldberg, D., 2002. Sonic waveform attenuation in gas hydrate-bearing sediments from the Mallik 2L-38 research well, Mackenzie Delta, Canada. J. Geophys. Res. Solid Earth 107 (B5). https://doi.org/10.1029/2001JB000556. EPM 1-1-EPM 1-11.
- Guo, Z.Q., Liu, C., Li, X.Y., et al., 2016. Modeling and analysis of frequency-dependent AVO responses in inelastic stratified media. Chin. J. Geophys. 59 (2), 664–672. https://doi.org/10.6038/cjg20160223 (in Chinese).
- Guo, Z.Q., Lv, X.Y., Liu, C., et al., 2022. Characterizing gas hydrate-bearing marine sediments using elastic properties—Part 1: rock physical modeling and inversion from well logs. J. Mar. Sci. Eng. 10 (10), 1379. https://doi.org/10.3390/ imse10101379.
- He, J.X., Ning, Z.J., Zhao, B., et al., 2022. Preliminary analysis and prediction of strategic replacement area for gas hydrate exploration in South China Sea. Earth Sci. 47 (5), 1549–1568. https://doi.org/10.3799/dqkx.2021.119 (in Chinese).
- Helgerud, M.B., Dvorkin, J., Nur, A., et al., 1999. Elastic-wave velocity in marine sediments with gas hydrates: effective medium modeling. Geophys. Res. Lett. 26 (13), 2021–2024. https://doi.org/10.1029/1999GL900421.
- Jafargandomi, A., Curtis, A., 2013. Assessing the seismic AVA detectability of CO₂ storage sites using novel time-lapse attributes. Pet. Geosci. 19 (4), 357–374. https://doi.org/10.1144/petgeo2012-043.
- Ji, A.S., Zhu, T.Y., Marín-Moreno, H., et al., 2021. How gas-hydrate saturation and morphology control seismic attenuation: a case study from the south Hydrate Ridge. Interpretation 9 (2), SD27–SD39. https://doi.org/10.1190/INT-2020-0137.1.
- Jin, J.P., Wang, X.J., Zhu, Z.Y., et al., 2023. Physical characteristics of high concentrated gas hydrate reservoir in the Shenhu production test area, South China Sea. Journal of Oceanology and Limnology 41 (2), 694–709. https://doi.org/10.1007/s00343-021-1435-9
- Kamei, R., 2012. Strategies for Visco-Acoustic Waveform Inversion in the Laplace-Fourier Domain, with Application to the Nankai Subduction Zone. Ph.D. Thesis, The University of Western Ontario, London, Canada, pp. 91–93. https://ir.lib.uwo.ca/etd/1061.
- Kleinberg, R.L., Flaum, C., Griffin, D.D., et al., 2003. Deep sea NMR: methane hydrate growth habit in porous media and its relationship to hydraulic permeability, deposit accumulation, and submarine slope stability. J. Geophys. Res. Solid Earth 108 (B10), 2508. https://doi.org/10.1029/2003JB002389.
- Li, C.H., Feng, K., Liu, X.W., 2013. Study on p-wave attenuation in hydrate-bearing sediments based on BISQ model. Journal of Geological Research 2013 (1), 176579. https://doi.org/10.1155/2013/176579.
- Li, C.H., 2015. Seismic Wave Attenuation in Hydrate-Bearing Sediments and the Estimates of Attenuation Coefficient. Ph.D. Thesis. China University of Geosciences, Beijing), Beijing (in Chinese).
- Li, C.H., Liu, X.W., 2017. Seismic wave attenuation in hydrate-bearing sediments based on the patchy saturation model in the Shenhu area, South China Sea. Interpretation 5 (3), SM25–SM32. https://doi.org/10.1190/INT-2016-0139.1.
- Li, J.F., Ye, J.L., Qin, X.W., et al., 2018. The first offshore natural gas hydrate production test in South China Sea. China Geology 1 (1), 5–16. https://doi.org/
- Li, Z.K., 2021. Elastic Wave Response Analysis on Thin Interbed of Marine Gas Hydrates. Master Thesis (in Chinese), China University of Geosciences (Beijing). https://doi.org/10.27493/d.cnki.gzdzy.2021.001294.
- Liang, J.Q., Deng, W., Lu, J.A., et al., 2020. A fast identification method based on the typical geophysical differences between submarine shallow carbonates and hydrate bearing sediments in the northern South China Sea. China Geology 3 (1), 16–27. https://doi.org/10.31035/cg2020021.
- Liu, L.F., Cao, S.Y., Wang, L., 2011. Poroelastic analysis of frequency-dependent amplitude-versus-offset variations. Geophysics 76 (3), C31–C40. https://doi. org/10.1190/1.3552702.
- Liu, C.L., Meng, Q.G., Li, C.F., et al., 2017. Characterization of natural gas hydrate and its deposits recovered from the northern slope of the South China Sea. Earth Sci. Front. 24 (4), 41–50. https://doi.org/10.13745/j.esf.yx.2016-12-35 (in Chinese).
- Liu, P.Q., 2022. Research on Gas Hydrate Identification Method Based on Seismic Wave Dispersion Characteristics. Ph.D. Thesis (in Chinese), China University of Petroleum (Beijing), p. 96. https://doi.org/10.27643/d.cnki.gsybu.2022.000001.
- Liu, B., Wang, X.J., Su, P.B., et al., 2024a. Identification of interbedded gas hydrate and free gas using amplitude versus offset forward modelling. Geophys. Prospect. 72, 1536–1552. https://doi.org/10.1111/1365-2478.13402.
- Liu, T., Bao, X.Y., Zhu, X.Y., et al., 2024b. Review of rock-physics studies on natural gas hydrate-bearing sediment attenuation. Reviews of Geophysics and Planetary Physics 55 (3), 369–380. https://doi.org/10.19975/j.dqyxx.2023-028 (in Chinese).
- Mavko, G., Mukerji, T., Dvorkin, J., 2009. In: The Rock Physics Handbook: Tools for Seismic Analysis of Porous Media, second ed. Cambridge University Press, New York, https://doi.org/10.1017/CB09780511626753.
- Meng, D.J., Wen, P.F., Zhang, R.W., et al., 2020. Gas hydrate S-wave velocity prediction method based on effective medium model. Oil Geophys. Prospect. 55 (1), 117–125. https://doi.org/10.13810/j.cnki.issn.1000-7210.2020.01.014 (in Chinese).
- Merey, S., Chen, L., 2022. Numerical comparison of different well configurations in the conditions of the 2020-gas hydrate production test in the Shenhu Area. Upstream Oil and Gas Technology 9, 100073. https://doi.org/10.1016/j.upstre.2022.100073.

Ning, F.L., Dou, X.F., Sun, J.X., et al., 2020. Progress in numerical simulation of sand production from hydrate reservoirs. Petroleum Science Bulletin 5 (2), 182–203. https://doi.org/10.3969/j.issn.2096-1693.2020.02.018 (in Chinese).

- Niu, B.H., Wen, P.F., Wen, N., et al., 2006. Estimation of hydrate concentration based on AVO modeling of BSR. Chin. J. Geophys. 49 (1), 143–152 (in Chinese).
 Pan, H.J., Li, Y.G., Wei, C., et al., 2022. Seismic rock-physics modeling of the
- Pan, H.J., Li, Y.G., Wei, C., et al., 2022. Seismic rock-physics modeling of the complex-morphology hydrate reservoirs and applications. Chin. J. Geophys. 65 (12), 4858–4873. https://doi.org/10.6038/cjg2022Q0185 (in Chinese).
- Pang, S., Liu, C., Guo, Z.Q., et al., 2018. Gas identification of shale reservoirs based on frequency-dependent AVO inversion of seismic data. Chin. J. Geophys. 61 (11), 4613–4624. https://doi.org/10.6038/cig2018L0529 (in Chinese).
- Picotti, S., Carcione, J.M., Rubino, J.G., et al., 2010. A viscoelastic representation of wave attenuation in porous media. Comput. Geosci. 36 (1), 44–53. https://doi.org/10.1016/j.cageo.2009.07.003.
- Ren, X.W., Guo, Z.Y., Ning, F.L., et al., 2020. Permeability of hydrate-bearing sediments. Earth Sci. Rev. 202, 103100. https://doi.org/10.1016/j.earscirev.2020.103100.
- Ruan, A.G., Li, J.B., Chu, F.Y., et al., 2006. AVO numerical simulation of gas hydrates reflectors beneath seafloor. Chin. J. Geophys. 49 (6), 1826–1835 (in Chinese). Sain, K., Singh, A.K., 2011. Seismic quality factors across a bottom simulating
- Sain, K., Singh, A.K., 2011. Seismic quality factors across a bottom simulating reflector in the makran accretionary prism, arabian sea. Mar. Petrol. Geol. 28 (10), 1838–1843. https://doi.org/10.1016/j.marpetgeo.2011.03.013.Santos, L.A., Matsumoto, R., Freitas, F.D.S., et al., 2023. Geophysical characterization
- Santos, L.A., Matsumoto, R., Freitas, F.D.S., et al., 2023. Geophysical characterization and attenuation correction applied for hydrate bearing sediments in Japan sea. Minerals 13 (5), 655. https://doi.org/10.3390/min13050655.
- Su, P.B., Lin, L., Lv, Y.Y., et al., 2022. Potential and distribution of natural gas hydrate resources in the South China Sea. J. Mar. Sci. Eng. 10 (10), 1364. https://doi.org/10.3390/jmse10101364.
- Tian, D.M., Liu, T., Liu, X.W., et al., 2021. Estimation of the gas hydrate saturation in the South China Sea. Arabian J. Geosci. 14 (14), 1408. https://doi.org/10.1007/s12517-021-07832-7.
- Tian, H.T., Liu, W.H., Ding, P.B., et al., 2024. Numerical simulation of elastic properties of hydrate-bearing sediments with digital rock technology. Mar. Petrol. Geol. 160, 106592. https://doi.org/10.1016/j.marpetgeo.2023.106592.
- Geol. 160, 106592. https://doi.org/10.1016/j.marpetgeo.2023.106592. Wang, X.J., Wu, S.G., Wang, J.L., et al., 2013. Anomalous wireline logging data caused by gas hydrate dissociation in the Shenhu area, northern slope of South China Sea. Chin. J. Geophys. 56 (8), 2799–2807. https://doi.org/10.6038/cjg20130828 (in Chinese).
- Wang, J.L., Wu, S.G., 2016. The characteristics of sonic wave attenuations of gas hydrate reservoirs at Well GC955H, Gulf of Mexico. Chin. J. Geophys. 59 (4), 1535–1542. https://doi.org/10.6038/cjg20160433 (in Chinese).
- Wang, W., Ba, J., Carcione, J.M., et al., 2021a. Wave properties of gas-hydrate bearing sediments based on poroelasticity. Front. Earth Sci. 9, 640424. https://doi.org/10.3389/feart.2021.640424.
- Wang, X.J., Jin, J.P., Guo, Y.Q., et al., 2021b. The characteristics of gas hydrate accumulation and quantitative estimation in the North Slope of South China Sea. Earth Sci. 46 (3), 1038–1057. https://doi.org/10.3799/dqkx.2020.321 (in Chinese).
- Wang, X.Y., 2022. Research on Seismic Rock Physics Model and Response Characteristics of Gas Hydrate-Bearing Sandstone Sediments. M.Eng. Thesis (in Chinese), Jilin University, Changchun, China, pp. 6–26. https://doi.org/10.27162/d.cnki.gilin.2022.000939.
- Wang, X.C., Sun, Y.H., Li, B., et al., 2023. Reservoir stimulation of marine natural gas hydrate-a review. Energy 263, 126120. https://doi.org/10.1016/j.energy.2022. 126120
- Wang, X.J., Han, L., Liu, J.Z., et al., 2025. Geophysical characteristics and identification of the coexistence of gas hydrate and free gas. Earth Sci. Front. 32 (2), 20–35 (in Chinese). https://link.cnki.net/urlid/11.3370.P.20240417.1503.010.
- Wei, J.G., Wu, T.T., Feng, X.L., et al., 2021. Physical properties of gas hydrate-bearing pressure core sediments in the South China Sea. Geofluids 2021, 6636125. https://doi.org/10.1155/2021/6636125.
- White, J.E., 1975. Computed seismic speeds and attenuation in rocks with partial gas saturation. Geophysics 40 (2), 224–232. https://doi.org/10.1190/1.1440520.
- Wu, C.Z., Zhang, F., Li, X.Y., 2022. Research progress of absorption and attenuation mechanism and petrophysical theory for gas hydrate reservoir. Oil Geophys. Prospect. 57 (4), 992–1008. https://doi.org/10.13810/j.cnki.issn.1000-7210.2022. 04.026 (in Chinese).
- Wu, C.Z., Han, L., Zhang, F., et al., 2023. Gas hydrate reservoir identification based on rock physics modelling and sensitive elastic parameters. J. Geophys. Eng. 20 (1), 117–127. https://doi.org/10.1093/jge/gxac100.
- Wu, C.Z., Zhang, F., Ding, P.B., et al., 2024. Rock-physics model of a gas hydrate reservoir with mixed occurrence states. Geophysics 89 (2), MR53–MR62. https://doi.org/10.1190/geo2023-0211.1.
- Xie, Y.F., Lu, J.A., Kuang, Z.G., et al., 2022. Well logging evaluation for three-phase zone with gas hydrate in the Shenhu area, South China Sea. Geoscience 36 (1), 182–192. https://doi.org/10.19657/j.geoscience.1000-8527.2021.167 (in Chinese).
- Xu, H.N., Zhang, G.X., Zheng, X.D., et al., 2014. Integrated analysis of well logs and seismic data to deduce the possible distribution in depth of gas hydrate in Shenhu Area, South China Sea. Chin. J. Geophys. 57 (10), 3363–3372. https:// doi.org/10.6038/cjg20141023 (in Chinese).
- Yang, S.X., Liang, J.Q., Lu, J.A., et al., 2017. Petrophysical evaluation of gas hydrate in Shenhu area, China. In: SPWLA 23rd Formation Evaluation Symposium of Japan.
- Ye, J.L., Qin, X.W., Xie, W.W., et al., 2020. The second natural gas hydrate production test in the South China Sea. China Geology 3 (2), 197–209. https://doi.org/10.31035/cg2020043.

- Zhan, L.S., Kang, D.J., Lu, H.L., et al., 2022. Characterization of coexistence of gas hydrate and free gas using sonic logging data in the Shenhu Area, South China Sea. J. Nat. Gas Sci. Eng. 101, 104540. https://doi.org/10.1016/j.jngse.2022.104540.
- Zhang, R.W., Li, H.Q., Wen, P.F., et al., 2016. The velocity dispersion and attenuation of marine hydrate-bearing sediments. Chin. J. Geophys. 59 (9), 3417–3427. https://doi.org/10.6038/cjg20160924 (in Chinese).

 Zhang, X.D., Yin, C., Zhang, G.L., 2021. Confirmation of AVO attribute inversion methods for gas hydrate characteristics using drilling results from the shenhu
- area, South China Sea. Pure Appl. Geophys. 178, 477-490. https://doi.org/ 10.1007/s00024-020-02653-3.
- Zhang, J., Gao, J.J., Wang, L.F., et al., 2024. Study on multicomponent Amplitude versus Offset forward modelling of thin layer gas hydrate using the Bre-khovskikh equation. Geophys. Prospect. 72 (4), 1350–1361. https://doi.org/ 10.1111/1365-2478.13375.
- Zhou, J.L., Wang, X.J., Zhu, Z.Y., et al., 2022. The influence of submarine landslides on the distribution and enrichment of gas hydrate and free gas. Chin. J. Geophys. 65 (9), 3674–3689. https://doi.org/10.6038/cjg2022P0957 (in Chinese).